Parametric Methods for Quantification of ^{18}F-FAZA Kinetics in Non–Small Cell Lung Cancer Patients

Eline E. Verwer[1], Idris Bahce[2], Floris H.P. van Velden[1], Maqsood Yaqub[1], Robert C. Schuit[1], Albert D. Windhorst[1], Pieter Raijmakers[1], Otto S. Hoekstra[1], Adriaan A. Lammertsma[1], Egbert F. Smit[2], and Ronald Boellaard[1]

[1]Department of Radiology and Nuclear Medicine, VU University Medical Center, Amsterdam, The Netherlands; and [2]Department of Pulmonary Diseases, VU University Medical Center, Amsterdam, The Netherlands

^{18}F-fluoroazomycinarabinoside (^{18}F-FAZA) is a hypoxia-specific PET tracer. In future clinical applications of hypoxia imaging, such as early response monitoring or radiation therapy dose painting, accurate quantification of tracer uptake at the voxel level will be required. The aim of the present study was to assess the validity of parametric methods for the quantification of ^{18}F-FAZA studies. **Methods:** Dynamic 70-min ^{18}F-FAZA scans were obtained from 9 non–small cell lung cancer patients. Arterial blood samples, collected at 7 time points, were used for preprocessing an image-derived input function derived from volumes of interest (VOIs) defined within the ascending aorta. Time–activity curves derived from various tumor VOIs were fitted using nonlinear regression analysis (NLR) to a reversible 2-tissue-compartment model, providing volumes of distribution (V_T) as an outcome measure. Next, parametric images were generated by use of both Logan graphic analysis with various linear regression start times and spectral analysis with multiple sets of basis functions. The previously defined tumor VOIs were projected onto these parametric images, and the resulting V_T were compared with those obtained from NLR. In addition, the results were compared with tumor-to-blood ratios (SUVr), which are more easily obtainable. **Results:** The highest correlations and correspondence with NLR-derived V_T were found for Logan graphic analysis with a start time of 30 min after injection (R^2, 0.88; intraclass correlation coefficient [ICC], 0.93) and for spectral analysis–derived V_T with a set of 30 basis functions with exponents ranging from 0.0175 to 1.9 (R^2, 0.79; ICC, 0.81). SUVr yielded similar correlations but showed significant bias at high V_T (R^2, 0.85; ICC, 0.80). **Conclusion:** Both Logan graphic analysis and spectral analysis yielded V_T that showed high correlations with nonlinear regression analysis–derived V_T. SUVr showed bias at high V_T.

Key Words: PET; hypoxia; non–small cell lung cancer; ^{18}F-FAZA; parametric images

J Nucl Med 2014; 55:1772–1777
DOI: 10.2967/jnumed.114.141846

Under hypoxic conditions, tumor cells are more resistant to radiation therapy (*1*) and their migratory and invasive potentials are increased (*2*). Imaging of hypoxia may aid in determining patient prognosis and selecting appropriate therapeutic strategies (*3–6*). In addition, mapping of hypoxic tumor areas may enable specific targeting of hypoxic tumor tissue with intensified radiation therapy (*7–9*).

^{18}F-fluoroazomycinarabinoside (^{18}F-FAZA) is a promising hypoxia-specific PET tracer (*10–15*) that is based on a nitroimidazole group and that undergoes electron reduction when it enters cells. Under normoxic conditions, this process is followed by reoxygenation and transport from the cell. In contrast, under hypoxic conditions, the tracer is retained because it binds to macromolecules within cells (*16*), leading to increased PET signal in areas containing hypoxic cells. However, the signal depends not only on the oxygenation status of the tissue under investigation but also on delivery (plasma concentration, blood flow, and extraction) and nonspecific uptake in tissue. For quantification of the degree of hypoxia, a tracer kinetic model that describes tracer kinetics in relation to delivery through the arterial circulation is needed.

In a previous study, a 2-tissue reversible model with a blood volume parameter ($2T4k+V_B$) was identified as the optimal model for describing ^{18}F-FAZA kinetics (*17*). Through nonlinear regression analysis (NLR), this model provided excellent fits to measured time–activity curves. Unfortunately, this method is markedly sensitive to noise and therefore is not suitable for analysis at the voxel level. However, the latter type of analysis may be useful given the expected heterogeneity in the distribution of hypoxia within a tumor.

Several methods for linearization have been proposed to reduce the sensitivity of the analysis to noise and enable voxel-level analysis, that is, to enable the generation of parametric images; these methods include spectral analysis (SA) (*18*), Patlak graphic analysis (*19*), and Logan graphic analysis (LGA) (*20*). The purpose of the present study was to assess the validity of these parametric methods for analyzing ^{18}F-FAZA data by comparing the results of parametric analyses and NLR in patients with non–small cell lung cancer. In addition, the results derived from parametric methods were compared with those derived from simplified methods because the latter methods would require a less elaborate imaging protocol.

MATERIALS AND METHODS

Inclusion Criteria

Patients aged 18 y and older were asked to participate in the study if they met the following criteria: histologically or cytologically proven non–small cell lung cancer with a lesion measuring at least 2.5 cm in diameter and located within 15 cm of the aortic arch

Received Apr. 17, 2014; revision accepted Aug. 11, 2014.
For correspondence or reprints contact: Eline E. Verwer, Department of Radiology and Nuclear Medicine, VU University Medical Center, P.O. Box 7057, 1007 MB Amsterdam, The Netherlands.
E-mail: e.verwer@vumc.nl
Published online Oct. 16, 2014.

and a hemoglobin level of at least 7.0 mmol/L. Exclusion criteria were chemotherapy or radiation therapy received within 6 mo before the PET study, pregnancy, and inability to remain supine for 100 min. The study was approved by the Medical Ethics Review Committee of the VU University Medical Center. Before inclusion, each patient signed a written protocol-specific informed consent form.

Data Acquisition

Scanning Protocol. Patients were scanned on a Gemini TF-64 PET/CT scanner (Philips). Each patient underwent a low-dose CT scan (50 mAs; 120 kVp), followed by a 70-min dynamic emission scan. The start time of the latter scan coincided with the beginning of an intravenous bolus injection of 168 ± 39 (mean ± SD) MBq of ^{18}F-FAZA with a specific activity of 143 ± 70 GBq·μmol^{-1}; the injection was administered and flushed with saline (5 mL at 0.8 mLs^{-1} and then 35 mL at 2 mLs^{-1}) using an automated pump system. PET data were normalized and corrected for dead time, randoms, scatter, and decay. Attenuation correction was based on the CT scan, and a 3-dimensional row-action maximum-likelihood reconstruction algorithm was used to reconstruct the data into 37 frames (1×10, 8×5, 4×10, 2×15, 3×20, 2×30, 6×60, 4×150, 4×300, and 3×600 s) with a matrix size of $144 \times 144 \times 45$ voxels (voxel size, $4 \times 4 \times 4$ mm). All data were reconstructed in accordance with recently published guidelines for quantitative ^{18}F-FDG PET studies (*21,22*).

Blood Sampling. At set time points (5, 10, 20, 30, 50, 60, and 70 min after injection), arterial blood samples were manually collected from a cannula inserted into the radial artery. These samples were analyzed for plasma–to–whole-blood ratios and for plasma fractions of parent ^{18}F-FAZA.

Kinetic Analysis

Multiple volumes of interest (VOIs) were defined within tumor tissue. Time–activity curves derived from these VOIs were fitted using NLR. The VOIs were also projected onto parametric images derived from dynamic PET data with LGA (*20*) and SA (*18*) and onto simplified parameter images derived from static PET imaging. The resulting VOI-based parameter values were compared.

NLR (Gold Standard). The governing equations for the 2T4k+V_B model are as follows (*23*):

$$\frac{dC_{ND}(t)}{dt} = K_1 C_P(t) - (k_2 + k_3) C_{ND}(t) + k_4 C_S(t), \qquad \text{Eq. 1}$$

$$\frac{dC_S(t)}{dt} = k_3 C_{ND}(t) - k_4 C_S(t), \qquad \text{Eq. 2}$$

and

$$C_T(t) = C_{ND}(t) + C_S(t), \qquad \text{Eq. 3}$$

where $C(t)$ represents the activity concentrations over time in tissue (C_T), in the first compartment (free tracer and nonspecifically bound tracer in tissue; C_{ND}), in the second compartment (specifically bound tracer in tissue; C_S), and in plasma after correction for metabolites (C_P). Because each VOI encompasses some blood volume, blood volume correction was applied with the following equation:

$$C_{PET}(t) = V_B C_{WB}(t) + (1 - V_B) C_T(t), \qquad \text{Eq. 4}$$

where V_B is the blood volume parameter, $C_{WB}(t)$ is the whole-blood time–activity curve, and $C_{PET}(t)$ is the tissue time–activity curve under consideration. For each time–activity curve, standard NLR routines (*24*) were used to derive estimates of V_B and rate constants K_1, k_2, k_3, k_4. Volumes of distribution (V_T) were then calculated with Equation 5:

$$V_T = \frac{K_1}{k_2}\left(1 + \frac{k_3}{k_4}\right). \qquad \text{Eq. 5}$$

Because NLR is sensitive to noise, for some time–activity curves the method was unable to produce reliable fits, particularly for small VOIs. V_T for these VOIs (18/96) were therefore excluded from further analysis.

LGA. In LGA (*20*), the governing differential equations for the reversible model are rearranged to yield

$$\frac{\int_0^t C_{PET}(\tau)d\tau}{C_{PET}(t)} = \alpha \frac{\int_0^t C_P(\tau)d\tau}{C_{PET}(t)} + \beta, \qquad \text{Eq. 6}$$

with

$$\alpha = V_B + (1 - V_B)\frac{K_1}{k_2}\left(1 + \frac{k_3}{k_4}\right) = V_B + (1 - V_B)V_T,$$

and

$$\beta = -\frac{(1 - V_B)}{k_2 k_4}\left(k_2 \frac{C_S(t)}{C_{PET}(t)} + (k_3 + k_4)\frac{C_T(t)}{C_{PET}(t)}\right).$$

For reversible kinetics, Equation 6 becomes linear after a certain time, when β becomes constant. The slope of the "Logan plot," α, then represents V_T, albeit without correction for the blood volume fraction. Parametric V_T images were generated from the dynamic PET data by linear regression fitting to the data in Equation 6, estimating α, for each voxel.

SA. SA (*18*) assumes that the solution to the governing equations can be described by a weighted sum of a set of predefined basis functions:

$$C_{PET}(t) = \sum_{i=1}^{n} \alpha_i e^{-\beta_i t} \otimes C_P(t) + V_B C_{WB}(t), \qquad \text{Eq. 7}$$

where the last term is added to correct for blood volume in VOIs. V_T and K_1 can then be derived from the amplitudes and exponents of the basis functions:

$$V_T = \frac{1}{(1 - V_B)} \sum_{i=1}^{n} \frac{\alpha_i}{\beta_i}, \qquad \text{Eq. 8}$$

and

$$K_1 = \frac{1}{(1 - V_B)} \sum_{i=1}^{n} \alpha_i. \qquad \text{Eq. 9}$$

Parametric V_T, K_1, and V_B images were generated by fitting Equation 7 to the dynamic PET data, estimating α_i and V_B values, for each voxel.

Simplified Methods. Of the simplified parameters, we chose to compare the results obtained from the parametric methods with tumor-to-blood ratios (SUVr), as we previously found SUVr to show the highest correspondence with NLR-derived V_T (*17*). SUVr images were derived from the average PET frames acquired at 50–60 min after injection; voxel-by-voxel activity concentrations were normalized to the blood activity concentrations obtained from a VOI within the ascending aorta.

Derivation of Plasma Input Functions. For each patient, a VOI (2–3 mL) within the ascending aorta was defined manually from an early

PET frame most clearly displaying the blood pool. The metabolite-corrected image-derived plasma input function (IDIF) was then derived from the corresponding time–activity curve, corrected for both plasma–to–whole-blood ratios and parent fractions obtained from the manually collected arterial blood samples, and calibrated to the whole-blood activity concentrations of the samples collected 50 min after injection as previously described by Verwer et al. (*17*).

Input Parameter Setting Selection and Validation

For the identification of appropriate input parameter settings, for each patient, VOIs were defined within the largest tumor structure visible on the low-dose CT image (whole tumor; whole tumor excluding edge voxels) and on the averaged image from the last 30 min of ^{18}F-FAZA data (whole tumor; within an area of relatively low activity concentrations; within an area of relatively high activity concentrations). All VOIs were modified manually to exclude large blood vessels visible on early PET frames. Time–activity curves derived from these VOIs were fitted with NLR to obtain V_T estimates. Parametric images were generated with LGA and SA for various input settings (Supplemental Tables 1 and 2; supplemental materials are available at http://jnm.snmjournals.org). Averaged V_T were obtained by projecting the VOIs onto the parametric images. The input parameter settings yielding the highest correlations between parametric method–derived and NLR-derived V_T were then selected for further analysis.

In addition, for assessment of whether the parametric methods were able to accurately quantify the heterogeneous distribution of tracer-specific uptake in tumor tissue, several (4–7) smaller VOIs were defined within areas showing marked heterogeneity. In particular, areas in which voxel-by-voxel differences were observed in V_T derived from LGA and V_T derived from SA were studied. Input parameter settings were then further refined on the basis of correlations and correspondence of the resulting V_T with NLR-derived V_T for these VOIs.

After the selection of appropriate input parameter settings for the parametric methods, VOI-based V_T, V_B, K_1, and SUVr estimates were derived for all tumor VOIs with the aforementioned methods and compared with the results of NLR, which was used as the gold standard.

Statistics

Statistical analysis was performed with the SPSS Statistics 20 (IBM) software package. For comparison of the results of the various methods, linear regression analysis was performed. Correlations were assessed with the Pearson correlation coefficient (R^2). Correspondence was assessed with the intraclass correlation coefficient (ICC). P values of less than 0.05 were considered significant. Bland–Altman plots were constructed to visualize correspondence and variability. Plots presented in this article were generated with Excel 2007 (Microsoft Corp.).

RESULTS

Patients

Nine patients (3 men and 6 women) ranging in age from 36 to 70 y were included in the study. The median patient weight was 78 kg (range, 59–91 kg), and the median height was 166 cm (range, 158–183 cm). The median size of the largest tumor structure in each patient was 67 mL (range, 9–312 mL). Figure 1 shows ^{18}F-FAZA PET/CT images from a typical patient with non–small cell lung cancer. A typical example of acquired blood data and the resulting IDIF is shown in Figure 2.

Kinetic Analysis and Validation

Parametric images were obtained from LGA and SA at various settings. Figure 3 shows representative V_T and SUVr images at the tumor level. Figure 4 shows scatterplots and regression lines for the results of regional comparisons of the various methods. For

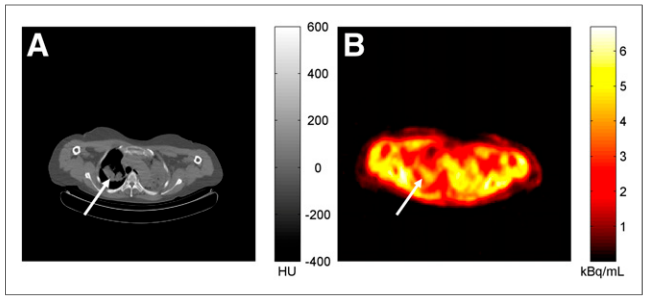

FIGURE 1. Axial images of typical patient diagnosed with non–small cell lung cancer. (A) Low-dose CT. (B) ^{18}F-FAZA averaged image for interval from 40 to 70 min after injection, illustrating tumor uptake. White arrow indicates location of tumor (tumor size, 76 mL). HU = Hounsfield units.

correlation of these results, 1 VOI was excluded, as the gold standard V_T (V_T derived from NLR) for this VOI was considered to be unrealistically high (2.06) compared with those for all other VOIs. However, because no obvious reason for the inaccuracy of this data point could be found in PET or blood data, the data point is shown in the scatterplots. For the sake of completeness, scatterplots and regression analysis results for data including this outlier are given in Supplemental Figure 1.

The best results for LGA were obtained with a start time of 30 min (R^2, 0.88; ICC, 0.93) (Fig. 4A; Supplemental Table 1). For SA, a set of 30 basis functions with exponents ranging from 0.0175 to 1.9 min^{-1} yielded the best results (R^2, 0.79; ICC, 0.81) (Fig. 4C; Supplemental Table 2). Better correlations were achieved by selecting different boundaries for the basis function exponents (e.g., an R^2 of 0.87 for exponents ranging from 0.01 to 3.0 min^{-1}). However, this approach also changed the slope of the regression line and decreased the absolute correspondence with NLR-derived V_T (ICC, 0.76). V_B values obtained from SA showed significant correlations with corresponding NLR results (R^2, 0.89; ICC, 0.93). K_1 values showed no correlation (R^2, 0.09).

Figure 4B shows comparisons of SUVr with V_T (R^2, 0.85; ICC, 0.80). Figure 4D shows the relative differences between V_T derived from LGA and V_T derived from SA as a function of V_B. A typical example of the relative differences at the voxel level is shown in Figure 3E. Figure 3F shows the relative differences between SUVr and SA-derived V_T. Bland–Altman plots for the various methods compared with NLR are given in Supplemental Figure 2.

DISCUSSION

^{18}F-FAZA is a nitroimidazole-based PET tracer for noninvasively assessing tumor tissue pO_2 levels. For ^{18}F-FAZA to be used for this purpose, accurate quantification of specific tracer uptake is required. The present study validated the use of 2 parametric methods for quantification at the voxel level.

All methods were compared with NLR. Because NLR is sensitive to noise, the comparison was VOI based. This approach could lead to quantification errors in areas with marked variations in PET signal because such variations could be averaged out. Because hypoxia is expected to be heterogeneously distributed within a tumor, so is ^{18}F-FAZA uptake. To take possible errors due to heterogeneity into consideration, we included in the analysis multiple smaller VOIs that were defined within areas of the tumor showing various characteristics (such as relatively high or low PET signal

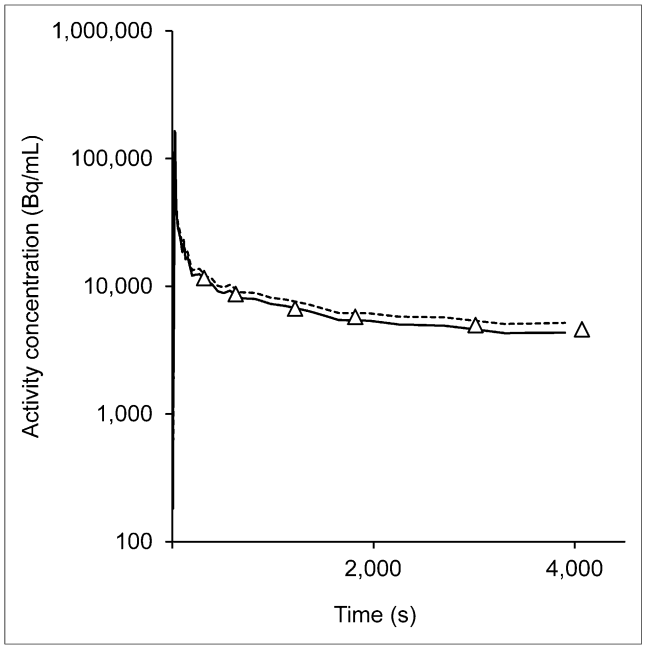

FIGURE 2. Blood data with time–activity curve derived from ascending aorta (dashed line), metabolite-corrected image-derived plasma input function (solid line), and whole-blood activity concentrations obtained from 6 manually collected arterial blood samples (△). For this patient, 1 blood sample was omitted for logistic reasons.

or differences in V_T derived from the 2 parametric methods). The results for these smaller VOIs were found to be consistent with those for the other VOIs.

Both parametric methods produced V_T showing high correlations with those obtained from a full kinetic analysis. However, as shown in Figures 3 and 4, some differences between the methods were observed. Figures 3D and 3E indicated that these differences might be explained by high blood volume fractions within voxels because LGA does not incorporate blood volume correction. Regional analysis, however, showed no correlation of V_B with differences between V_T derived from LGA and V_T derived from SA.

LGA performed well (R^2, 0.88; ICC, 0.93), although some increased variability was observed at relatively low as well as relatively high V_T. A possible explanation is that even though a start time of 30 min generally led to the highest correlation with NLR-derived V_T, for some VOIs, particularly those with high V_T, the second term in Equation 6 might not yet have been constant at that start time. The observed bias at high V_T can indeed be decreased by selection of a later start time (e.g., 40 min after injection) (Supplemental Fig. 3), but this approach leads to errors for other VOIs. Another explanation is noise-induced bias. LGA is known to have noise-induced bias, particularly at high V_T, causing underestimation (*25*). LGA performance could be somewhat improved (R^2, 0.90; ICC, 0.94) by fitting Equation 6 with orthogonal regression analysis (*26*).

SA results showed high correspondence with NLR-derived V_T (R^2, 0.79; ICC, 0.81). The disadvantages of SA are the sensitivity of the method to minor changes in input parameters and long computing times (~10 times longer than LGA). As shown in Supplemental Figure 2, SA results were more variable than LGA results; this finding was expected because more parameters need to be estimated in SA. However, SA also has advantages. V_B values correlated highly with those obtained from NLR (R^2, 0.89). Calculating V_B may be useful as a quality assurance step and for providing information on tumor vascularity. Estimates of K_1 by SA and NLR were markedly sensitive to noise. For the final selection of input parameters, no correlation was found between SA-derived and NLR-derived K_1 values (R^2, 0.09) when all VOIs were considered. Correlation was improved when the analysis was limited to larger VOIs (R^2 for VOI sizes of >10 mL, 0.52), illustrating the influence of noise on estimates of K_1 with SA.

Both parametric methods required an elaborate imaging protocol consisting of dynamic PET imaging and blood sampling. For ^{18}F-FAZA, use of the IDIF in combination with venous blood sampling instead of (continuous) arterial blood sampling has been validated (*17*), simplifying the protocol. However, the need for venous blood sampling and metabolite analysis may still limit the clinical applicability of the presented methods. In the study of Verwer et al. (*17*), metabolite formation was observed to be slow, plasma-to-blood ratios were typically equal to 1, and both measures showed limited interpatient variability. Indeed, omission of the corrections for plasma-to-blood ratios and parent fractions led to an underestimation of V_T by only 8%. These findings need to be further substantiated under various clinical conditions but hint at the possibility of using the whole-blood IDIF, which would improve the clinical feasibility of the acquisition protocol.

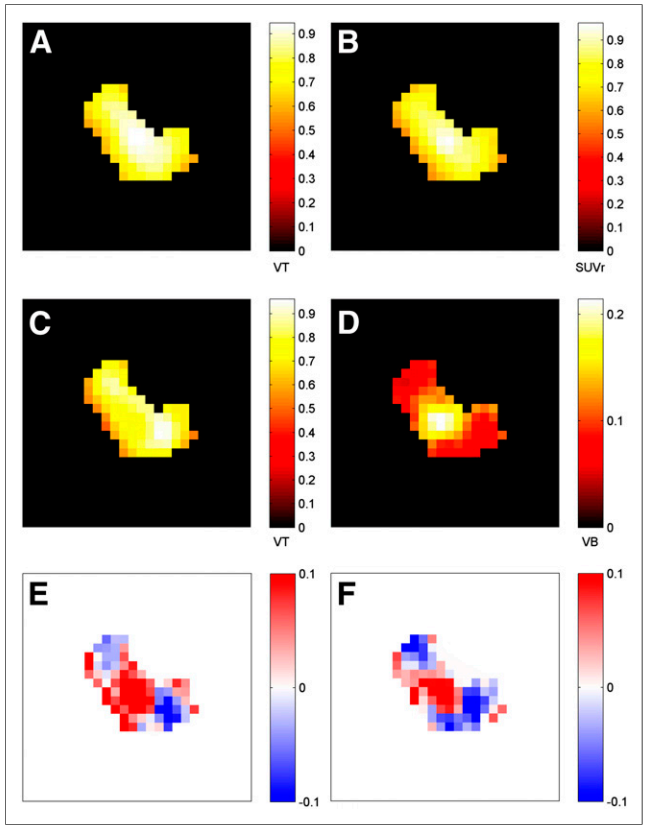

FIGURE 3. Typical examples of parametric images for whole-tumor VOIs. (A) V_T derived from LGA with start time of 30 min after injection. (B) SUVr based on PET data acquired 50–60 min after injection. (C and D) V_T (C) and V_B (D) derived from SA with input response function consisting of weighted sum of 30 basis functions and exponents ranging from 0.0175 to 1.9. (E and F) Relative differences between LGA-derived V_T and SA-derived V_T (E) and between SUVr and SA-derived V_T (F), where relative difference was calculated as $[(V_{T,\ LGA}$ or SUVr $- V_{T,SA})/(V_{T,\ LGA}$ or SUVr $+ V_{T,SA}) \cdot 2]$.

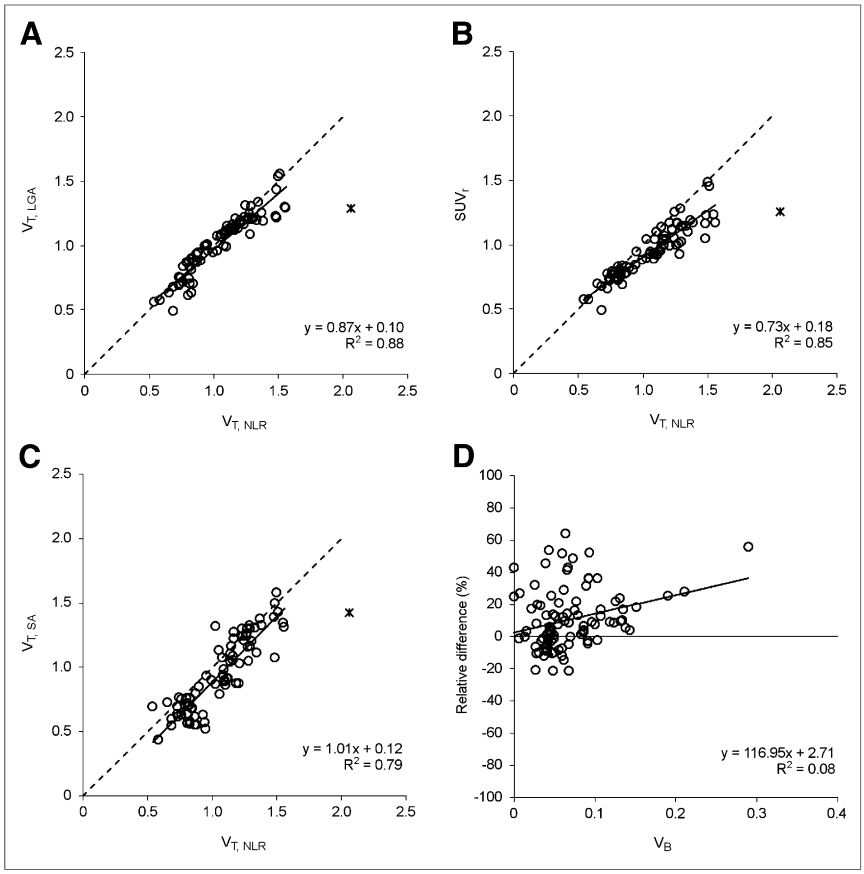

FIGURE 4. (A–C) Regional V_T for all tumor VOIs obtained from LGA ($V_{T,LGA}$) (A), regional SUVr (B), and SA ($V_{T,SA}$) (C) as function of V_T derived from NLR ($V_{T,NLR}$). (D) Differences between V_T derived from SA and V_T derived from LGA {percentage relative difference was calculated as $[(V_{T,LGA} - V_{T,SA})/(V_{T,LGA} + V_{T,SA}) \times 200]$} as function of V_B derived from NLR. Solid line = regression line through all data points, excluding 1 suspected outlier (*). Dashed line = line of identity.

Nevertheless, in routine clinical settings, a static imaging protocol may be preferable because dynamic imaging generally requires longer imaging times and may therefore be more costly and more prone to artifacts related to patient motion. Therefore, SUVr was also investigated. For calculation of SUVr, typically a short-duration (e.g., 10-min) static PET/CT scan is acquired at a late time point (>50 min after injection). Tumor tissue and blood activity concentrations are then derived from the PET image directly. The blood pool will not be clearly visible on the late PET image, but this characteristic will not be a limitation with respect to deriving blood activity concentrations because the ascending aorta and aortic arch are clearly identifiable on the low-dose CT image. However, it can lead to considerable quantification errors caused by the blood volume in the tumor tissue VOIs because SUVr does not correct for V_B (Fig. 3F). In the present analysis, VOIs were manually adjusted to exclude areas of markedly high V_B (i.e., visible blood vessels) by use of early PET frame data, thereby reducing potential errors caused by high V_B. With a static imaging protocol, this quality assurance step cannot be performed. In future applications, this limitation of SUVr should be considered. In the present analysis, regional SUVr estimates showed high correlations with NLR-derived V_T (R^2, 0.85) but significant negative bias, particularly at high V_T.

Which method should be used in clinical settings ultimately depends on the clinical objective. For assessing whether tumor tissue is hypoxic or not, defining a suitable threshold for the quantification parameter used could be sufficient. Depending on the threshold, systematic bias and underestimation at high V_T (like those observed with SUVr) might not affect clinical conclusions. In that situation, SUVr would be the method of choice because both the method and the acquisition protocol are straightforward. Large clinical trials relating quantification parameter values to clinical outcomes are needed to assess whether the observed bias in SUVr results in clinically relevant quantification errors. For purposes requiring more detailed information, such as radiation dose painting and early response monitoring (for which the ability to assess minor variations is essential), accurate voxel-by-voxel quantification is required. In such scenarios, parametric methods are recommended. SA is more versatile than LGA but shows larger variability. On the other hand, LGA results may be affected by the lack of blood volume correction. However, the effect will be less pronounced for LGA than for SUVr because with LGA, early PET frame data are available for excluding large blood volume regions.

Even though the parametric methods performed well in the present study, clinical conditions are likely to change over the course of a response monitoring study. Longitudinal trials are needed to evaluate the robustness of the methods under various clinical conditions. It would also be of interest to directly compare ^{18}F-FAZA voxel V_T derived from the parametric methods with localized pO_2 needle electrode measurements to assess the relationship between V_T and tissue pO_2 levels. However, such a study would be invasive and feasible only for superficial tumor structures.

CONCLUSION

Both LGA and SA produced accurate V_T images for the quantification of ^{18}F-FAZA. Additionally, the latter also produced accurate V_B values. SUVr also correlated well with NLR-derived V_T but showed significant bias, particularly at high V_T.

DISCLOSURE

The costs of publication of this article were defrayed in part by the payment of page charges. Therefore, and solely to indicate this fact, this article is hereby marked "advertisement" in accordance with 18 USC section 1734. This study was performed within the framework of the Center for Translational Molecular Medicine (AIRFORCE project; grant 03O-103). No other potential conflict of interest relevant to this article was reported.

ACKNOWLEDGMENTS

We thank our colleagues at the Department of Radiology and Nuclear Medicine and all patients who participated in the study.

REFERENCES

1. Gray LH, Conger AD, Ebert M, et al. The concentration of oxygen dissolved in tissues at the time of irradiation as a factor in radiotherapy. *Br J Radiol.* 1953; 26:638–648.
2. Vaupel P, Mayer A. Hypoxia in cancer: significance and impact on clinical outcome. *Cancer Metastasis Rev.* 2007;26:225–239.
3. Mortensen LS, Johansen J, Kallehauge J, et al. FAZA PET/CT hypoxia imaging in patients with squamous cell carcinoma of the head and neck treated with radiotherapy: results from the DAHANCA 24 trial. *Radiother Oncol.* 2012;105:14–20.
4. Beck R, Roper B, Carlsen JM, et al. Pretreatment ^{18}F-FAZA PET predicts success of hypoxia-directed radiochemotherapy using tirapazamine. *J Nucl Med.* 2007;48:973–980.
5. Eschmann SM, Paulsen F, Reimold M, et al. Prognostic impact of hypoxia imaging with ^{18}F-misonidazole PET in non–small cell lung cancer and head and neck cancer before radiotherapy. *J Nucl Med.* 2005;46:253–260.
6. Rischin D, Hicks RJ, Fisher R, et al. Prognostic significance of [^{18}F]-misonidazole positron emission tomography-detected tumor hypoxia in patients with advanced head and neck cancer randomly assigned to chemoradiation with or without tirapazamine: a substudy of Trans-Tasman Radiation Oncology Group Study 98.02. *J Clin Oncol.* 2006;24:2098–2104.
7. Arabi M, Piert M. Hypoxia PET/CT imaging: implications for radiation oncology. *Q J Nucl Med Mol Imaging.* 2010;54:500–509.
8. Krohn KA, Link JM, Mason RP. Molecular imaging of hypoxia. *J Nucl Med.* 2008;49(suppl 2):129S–148S.
9. Grosu AL, Souvatzoglou M, Roper B, et al. Hypoxia imaging with FAZA-PET and theoretical considerations with regard to dose painting for individualization of radiotherapy in patients with head and neck cancer. *Int J Radiat Oncol Biol Phys.* 2007;69:541–551.
10. Bollineni VR, Kerner GSMA, Pruim J, et al. PET imaging of tumor hypoxia using ^{18}F-fluoroazomycin arabinoside in stage III–IV non–small cell lung cancer patients. *J Nucl Med.* 2013;54:1175–1180.
11. Souvatzoglou M, Grosu AL, Roper B, et al. Tumour hypoxia imaging with [^{18}F]FAZA PET in head and neck cancer patients: a pilot study. *Eur J Nucl Med Mol Imaging.* 2007;34:1566–1575.
12. Postema EJ, McEwan AJ, Riauka TA, et al. Initial results of hypoxia imaging using 1-α-D-(5-deoxy-5-[^{18}F]-fluoroarabinofuranosyl)-2-nitroimidazole (^{18}F-FAZA). *Eur J Nucl Med Mol Imaging.* 2009;36:1565–1573.
13. Shi K, Souvatzoglou M, Astner ST, et al. Quantitative assessment of hypoxia kinetic models by a cross-study of dynamic ^{18}F-FAZA and ^{15}O-H_2O in patients with head and neck tumors. *J Nucl Med.* 2010;51:1386–1394.
14. Havelund BM, Holdgaard PC, Rafaelsen SR, et al. Tumour hypoxia imaging with ^{18}F-fluoroazomycinarabinofuranoside PET/CT in patients with locally advanced rectal cancer. *Nucl Med Commun.* 2013;34:155–161.
15. Trinkaus ME, Blum R, Rischin D, et al. Imaging of hypoxia with ^{18}F-FAZA PET in patients with locally advanced non-small cell lung cancer treated with definitive chemoradiotherapy. *J Med Imaging Radiat Oncol.* 2013;57:475–481.
16. Nunn A, Linder K, Strauss HW. Nitroimidazoles and imaging hypoxia. *Eur J Nucl Med.* 1995;22:265–280.
17. Verwer EE, van Velden FH, Bahce I, et al. Pharmacokinetic analysis of [^{18}F]FAZA in non-small cell lung cancer patients. *Eur J Nucl Med Mol Imaging.* 2013;40: 1523–1531.
18. Cunningham VJ, Jones T. Spectral analysis of dynamic PET studies. *J Cereb Blood Flow Metab.* 1993;13:15–23.
19. Patlak CS, Blasberg RG, Fenstermacher JD. Graphical evaluation of blood-to-brain transfer constants from multiple-time uptake data. *J Cereb Blood Flow Metab.* 1983;3:1–7.
20. Logan J, Fowler JS, Volkow ND, et al. Graphical analysis of reversible radioligand binding from time-activity measurements applied to [*N*-^{11}C-methyl]-(−)-cocaine PET studies in human subjects. *J Cereb Blood Flow Metab.* 1990;10: 740–747.
21. Boellaard R. Standards for PET image acquisition and quantitative data analysis. *J Nucl Med.* 2009;50(suppl 1):11S–20S.
22. Boellaard R, O'Doherty MJ, Weber WA, et al. FDG PET and PET/CT: EANM procedure guidelines for tumour PET imaging—version 1.0. *Eur J Nucl Med Mol Imaging.* 2010;37:181–200.
23. Gunn RN, Gunn SR, Cunningham VJ. Positron emission tomography compartmental models. *J Cereb Blood Flow Metab.* 2001;21:635–652.
24. Yaqub M, Boellaard R, Kropholler MA, et al. Optimization algorithms and weighting factors for analysis of dynamic PET studies. *Phys Med Biol.* 2006; 51:4217–4232.
25. Slifstein M, Laruelle M. Effects of statistical noise on graphic analysis of PET neuroreceptor studies. *J Nucl Med.* 2000;41:2083–2088.
26. Varga J, Szabo Z. Modified regression model for the Logan plot. *J Cereb Blood Flow Metab.* 2002;22:240–244.